

EVALUATION OF THE MPD DETECTOR CAPABILITIES FOR THE STUDY OF THE STRANGENESS PRODUCTION AT THE NICA COLLIDER

M. A. Ilieva^a, *V. I. Kolesnikov*^a, *Yu. A. Murin*^a, *D. A. Suvarieva*^a,
V. A. Vasendina^a, *A. I. Zinchenko*^{a, 1}, *E. I. Litvinenko*^a, *K. K. Gudima*^b

^a Joint Institute for Nuclear Research, Dubna

^b Institute of Applied Physics of the Academy of Sciences of Moldova, Chisinau

One of the main tasks of the NICA/MPD physics program is the study of the strangeness production in nuclear collisions. In this paper the MPD detector performance is presented for measurements of K_S^0 mesons, $\Lambda(\bar{\Lambda})$ hyperons, and hypertritons in central Au + Au collisions at NICA energies.

Одной из основных задач физической программы эксперимента MPD на комплексе NICA является изучение рождения странности в ядерных взаимодействиях. В данной работе представлены возможности детектора MPD по измерению K_S^0 -мезонов, $\Lambda(\bar{\Lambda})$ -гиперонов и гипертрионов в центральных взаимодействиях Au + Au при энергиях NICA.

PACS: 14.20.Jn; 14.40.-n

INTRODUCTION

The primary goal of the NICA (Nuclotron-based Ion Collider Facility) heavy-ion program [1] is the study of the properties of nuclear matter under extreme conditions. At sufficiently high temperature and baryon density achieved in central collisions of relativistic nuclei, a transition into a state of deconfined quarks and gluons — quark gluon plasma (QGP) — is expected. In the dense nuclear matter, the deconfinement phase transition might be accompanied by a restoration of chiral symmetry due to melting of the quark condensate [2–4]. Recent results on hadroproduction from the CERN SPS [5] and RHIC [6] indicate that the onset of the deconfinement is likely to be observed in central $A + A$ collisions at energies $\sqrt{s} > 7A$ GeV. Moreover, the analysis of the thermodynamic freeze-out parameters extracted from the data over a wide energy range performed in [7] reveals that the net-baryon density in central collisions of heavy ions has a maximum in the energy range from $\sqrt{s} = 5A$ to $9A$ GeV. So, the energy range of the NICA collider ($4A < \sqrt{s} < 11A$ GeV) is ideal for an experimental exploration of fundamental QCD properties that are sensitive to both the phenomena: chiral symmetry and confinement [8]. Our experimental research plan is to perform

¹E-mail: Alexander.Zinchenko@jinr.ru

a detailed energy scan with ion beams from protons to gold nuclei addressing the following objectives: (1) strangeness production, (2) in-medium properties of vector mesons, (3) event-by-event fluctuations, and (4) correlations. The measurements will be performed with the MultiPurpose Detector (MPD) [9,10] capable of detecting both the hadronic ($\pi, K, p, \Lambda, \Xi, \Omega$) and nonhadronic (e, γ) probes.

Study of (anti)hyperon production is of particular interest because of several reasons. First of all, the strangeness enhancement in heavy-ion collisions relative to proton-induced reactions has been proposed as a signature for the deconfinement. The expected increase of the strange particle production in a QGP phase is due to both the lower threshold of the $s\bar{s}$ -pair production and the addition of gluon fragmentation channels [11]. It was also established experimentally that this strangeness enhancement is stronger for particles with higher strangeness content [12,13].

Secondly, since the hadronic cross sections of multistrange hyperons are small, additional rescattering effects in the dense hadronic matter for strange hadrons are not so important as for other hadrons. Thus, measured phase-space distributions of strange hyperons reveal important characteristics of the fireball at the early stages of the system evolution. Moreover, it has recently been observed by the STAR experiment that the characteristic azimuthal anisotropy pattern (e.g., the elliptic flow coefficient v_2 as a function of transverse momentum p_t) for antibaryons (including those with strangeness) is different from the one for baryons in mid-central Au + Au collisions at energies $\sqrt{s} < 11A$ GeV [14]. Antibaryons are strongly affected by the comoving baryon density in the course of the reaction: there is an interplay between particle production and subsequent absorption in the medium. So, new experimental data on (anti)hyperon production which will be taken at NICA for different values of the collision energy and beam atomic mass number will provide a valuable insight into the reaction dynamics.

Relativistic heavy-ion collisions, where lots of strange particles (kaons and hyperons) are produced, offer a unique possibility to create exotic nuclear objects with strangeness — hypernuclei [15]. Recently, the first results on the production of (anti)hypertritium in relativistic Au + Au collisions at RHIC and the LHC have been reported by the STAR and ALICE experiments [16,17]. The mechanism and dynamics of hypernuclei formation are not well understood — several approaches are suggested to explain their production rates: coalescence of lambdas with nucleons at midrapidity [18], thermal models [19], or absorption of some of the produced hyperons by the residual spectator nuclei [20]. To distinguish between different models, new experimental data on hypernuclei production taken in different initial conditions (i.e., collision energy and impact parameter) over large phase space are needed. The energy range of the NICA research program covers the region of the maximal baryon density where the production rates of nuclear clusters with strangeness are predicted to be enhanced considerably: as many as $3 \cdot 10^{-2}$ of ${}^3_{\Lambda}\text{H}$ and $1 \cdot 10^{-5}$ of ${}^5_{\Lambda\Lambda}\text{He}$ per unit of rapidity are expected in a central Au + Au collision at $\sqrt{s} = 5A$ GeV [19]. With a typical event rate of 6 kHz for the design NICA luminosity of $10^{27} \text{ cm}^{-2} \cdot \text{s}^{-1}$ a detailed study of the production mechanism of single hypernuclei as well as an observation of double hypernuclei at NICA look feasible.

The goal of this work was to study the performance of the MPD detector for (anti)hyperon and hypernuclei measurements in heavy-ion collisions at NICA. The emphasis was placed on the MPD particle identification capability for hadrons and light nuclei, reconstruction of secondary vertices, and background suppression in $\Lambda(\bar{\Lambda})$ and ${}^3_{\Lambda}\text{H}$ signal.

1. DETECTOR GEOMETRY

The detailed description of the MPD geometry can be found in [9,10]. The present analysis is based on the detectors covering the midrapidity region ($|\eta| < 1.3$): the main tracker Time Projection Chamber (TPC) and barrel Time-Of-Flight system (TOF), comprising a so-called start version, and takes into account up-to-date modifications of the detector design. The overall detector material budget can be seen in Fig. 1. One can see that the main material contribution comes from TPC inner and outer cages which are multilayer structures made of composite materials like kevlar and tedlar with high strength and long radiation length. The total amount of the material does not exceed 10% of the radiation length in the region of interest.

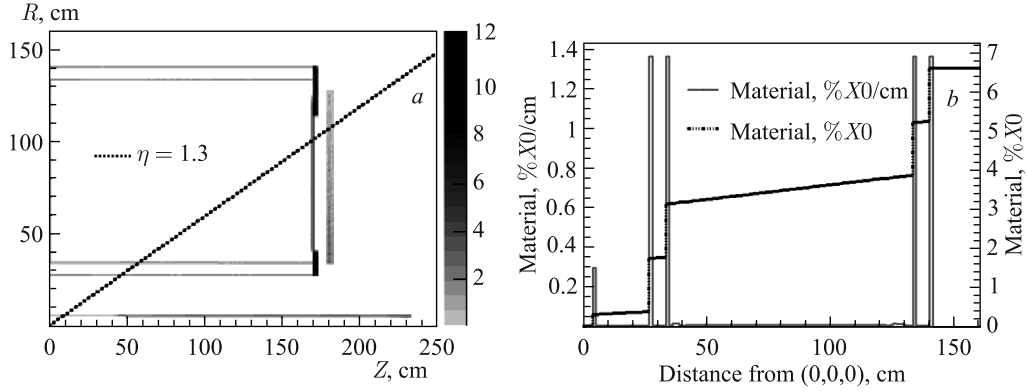


Fig. 1. *a*) Detector material budget in percent of radiation length X_0 . Z and R are the longitudinal and radial coordinates, measured from the detector center (point $(0,0,0)$); the dashed line corresponds to pseudorapidity $\eta = 1.3$ (detector acceptance limit considered). *b*) The detector material vs distance from the detector center at $\eta = 0$. The solid histogram and left scale correspond to the differential distribution, i.e., $\partial(\text{material})/\partial(\text{distance})$, the dashed histogram and right scale are for cumulative distribution, i.e., total material seen from the center. The spikes in the differential distribution correspond to the beam pipe ($R = 5$ cm), inner and outer TPC walls ($R \simeq 30$ and 140 cm)

2. EVENT GENERATORS AND DATA SETS

The event samples used for the present study were produced with the UrQMD [21] and DCM-QGSM (Dubna Cascade Model – Quark-Gluon String Model) [22–24] generators. It is well known that predictions of different models for the rapidity and transverse momentum distributions of hadrons (hyperons, in particular) can be different. Moreover, the differences among the model predictions can vary with the collision energy. If a detector's acceptance has limited rapidity and/or transverse momentum coverage (as is the case for the MPD setup), then the results of detector performance studies in terms of the overall reconstruction efficiency can vary from model to model as well. Therefore, in order to avoid a bias in the estimates of the detector performance, it looks reasonable to use several models with different predictions for the rapidity and p_T spectra of particles as an input for simulation. Moreover, the usage

of several event generators would allow one to estimate the detector sensitivity to the model predictions.

The choice of the aforementioned event generators was motivated by the following considerations: while the former is widely used by the heavy-ion community, the latter is able to produce nuclear clusters, in particular, hypernuclei, which were one of the subjects of this study, according to the prescription briefly presented below.

The DCM-QGSM generator is based on the Monte Carlo solution of a set of the Boltzmann–Uehling–Uhlenbeck relativistic kinetic equations with the collision terms, including cascade–cascade interactions. For particle energies below 1 GeV it considers only nucleons, pions, and deltas. The model includes a proper description of pion and baryon dynamics for particle production and absorption processes. At energies higher than about 5 GeV, the Quark–Gluon String Model is used to describe elementary hadron collisions. QGSM considers two lowest $SU(3)$ multiplets in mesonic, baryonic, and antibaryonic sectors, so interactions between almost 70 hadron species are treated on the same footing. The above-noted two energy extremes were bridged by the QGSM extension downward in the beam energy using the mix-and-match method.

During a collision of heavy ions, strangeness is produced abundantly and is likely to form clusters of different sizes. One can discriminate two distinct mechanisms for hypercluster formation in heavy-ion collisions. First, the absorption of hyperons in the spectator fragments of noncentral collisions. In this scenario one is interested in hyperons which propagate

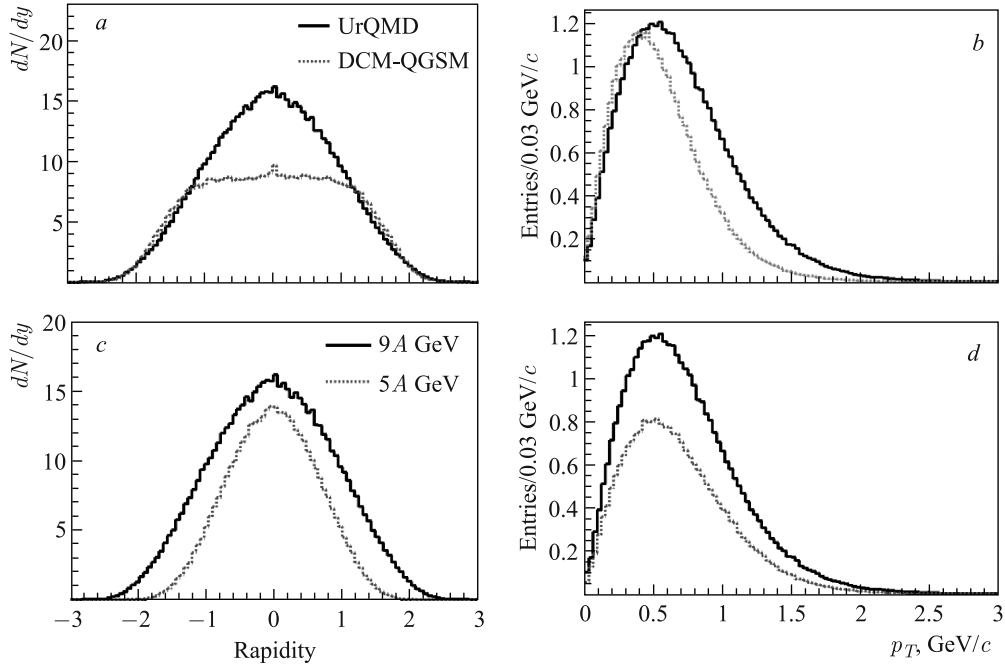


Fig. 2. *a, b*) Rapidity and p_T distributions of all (primary and secondary) Λ hyperons from UrQMD and DCM-QGSM generators at $\sqrt{s} = 9A$ GeV; *c, d*) rapidity and p_T distributions of all Λ hyperons from UrQMD generator at $\sqrt{s} = 5A$ and $9A$ GeV

with velocities close to the initial velocities of the nuclei, i.e., in the vicinity of nuclear spectators [25]. In this case one can obtain a rather large and moderately excited hyper-system decaying into hyperfragments later on [26]. In the other scenario the DCM-QGSM transport model gives the phase-space information for all hadrons produced in heavy-ion collisions. This information then serves as an input for coalescence prescription.

DCM-QGSM model predictions for cluster formation were compared with experimental data [27,28]. The model has been used to predict cluster production over a wide range of beam energies [20].

The two generators were used to produce event samples of central Au–Au collisions (0–3.0 fm in UrQMD and 0–3.8 fm in DCM-QGSM) at $\sqrt{s} = 5A$ and $9A$ GeV. The number of events ranged from 10^4 to $5 \cdot 10^5$, corresponding to about 30 s to 30 min of data taking time with the NICA design luminosity of $10^{27} \text{ cm}^{-2} \cdot \text{s}^{-1}$ (the corresponding central collision rate of ~ 300 Hz). One can see the model predictions for Λ hyperons in Fig. 2. The plots show distributions for all Λ hyperons, i.e., the primary (from the Au + Au collision) and secondary (produced during the particle transport within 50 cm from the collision point, i.e., from, e.g., Σ^0, Ξ^- and Ω^- decays). It should be noted here that we did not intend to do a detailed comparison of the model predictions on hyperon production; therefore, one should not pay too much attention to the differences in Fig. 2 which might eventually go away after proper model parameter tuning.

Particles produced by the event generators have been transported through the detector using the GEANT3 transport package (describing particle decays, secondary interactions, etc.). The decay properties of hypernuclei (modes and branching ratios) have been introduced into GEANT from [29] (Table 1) and the lifetime has been taken to be the same as of Λ hyperon.

Table 1. ${}^3_\Lambda\text{H}$ decays. The decay modes which were studied are marked in bold

Decay channel	Branching ratio, %
$\pi^- + {}^3\text{He}$	24.7
$\pi^0 + {}^3\text{H}$	12.4
$\pi^- + p + d$	36.7
$\pi^0 + n + d$	18.4
$\pi^- + p + p + n$	1.5
$\pi^0 + n + n + p$	0.8
$d + n$	0.2
$p + n + n$	1.5

3. DETECTOR PERFORMANCE

3.1. Track Reconstruction. The track reconstruction method is based on the Kalman filtering technique (see, e.g., [30]) and the number of TPC points per track was required to be greater than 10 to ensure a good precision of momentum and dE/dx measurements. In addition, we have restricted our study to the midrapidity region with $|\eta| < 1.3$. The track finding efficiency in TPC for primary and secondary tracks is shown in Fig. 3 as a function of the track transverse momentum. The secondary track sample there included particles produced within 50 cm of the primary vertex in both transverse and longitudinal directions and did not include electrons and positrons from the photon conversion, which were not relevant for the current study.

In spite of the fact that the amount of the material in front of the TPC active volume is rather small (below 4% — see Fig. 1, *b*), its effect on the momentum resolution for low- p_T tracks is quite visible especially for heavy particles (see Fig. 4, *a* for protons). However, the energy losses can be accounted for in the track fitting procedure. The transverse momentum

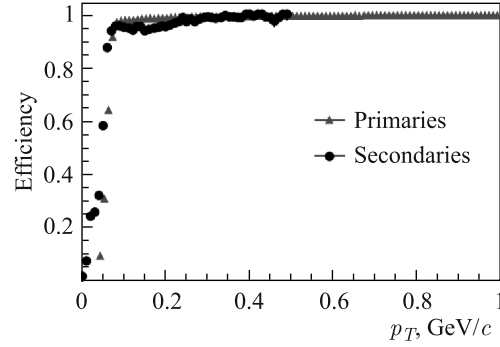


Fig. 3. Track reconstruction efficiency as a function of track p_T for primary and secondary particles

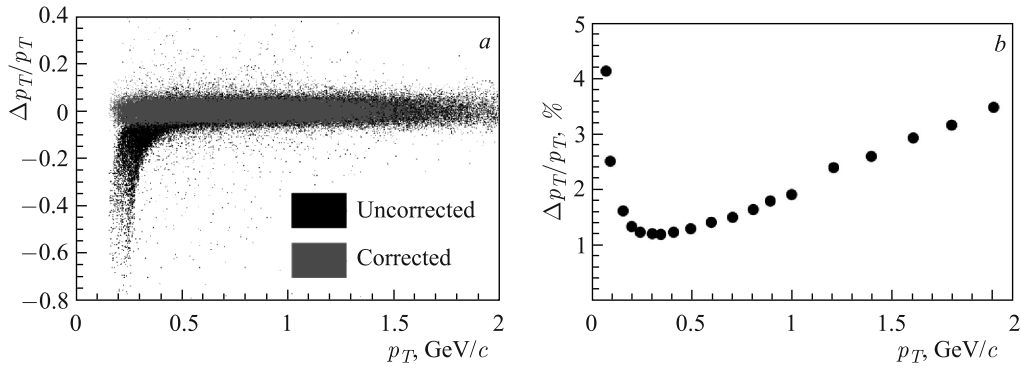


Fig. 4. *a*) Relative transverse momentum error versus p_T for protons before (black dots) and after (gray ones) corrections for energy losses in the TPC inner walls; *b*) relative transverse momentum resolution for primary tracks with $|\eta| < 1.3$ reconstructed in TPC

resolution after the corrections as a function of p_T can be seen in Fig. 4, *b*. The result was obtained with the assumption on the TPC coordinate resolution of 0.5 and 1.0 mm in transverse and longitudinal directions, respectively. Figure 5, *a* shows the transverse and longitudinal position uncertainties of primary tracks at their point of the closest approach to the interaction point versus track momentum. These detector characteristics are important for secondary vertex reconstruction.

Both the primary and secondary vertex reconstruction methods utilized make use of a similar approach based on the Kalman filtering formalism [31]. The primary vertex reconstruction errors as functions of the track multiplicity in the event are shown in Fig. 5, *b*.

For all the tracks reconstructed in the TPC the specific energy loss dE/dx is calculated as a truncated mean of the charges of the TPC hits assigned to the tracks. The truncation level of 70% was chosen; i.e., 30% of hits with the highest charges were excluded from the mean value.

Next, the TPC reconstructed tracks are extrapolated to the TOF detector and matched to the TOF hits. Figure 6 shows the TOF matching efficiency as a function of transverse momentum (plot *a*) and pseudorapidity (plot *b*). Relatively large uncertainty of the direction of reconstructed tracks (due to multiple scattering) causes the observed drop in the TPC–TOF matching efficiency at low p_T (see Fig. 6, *a*). Midrapidity tracks (at $\eta \approx 0$) are less efficiently matched

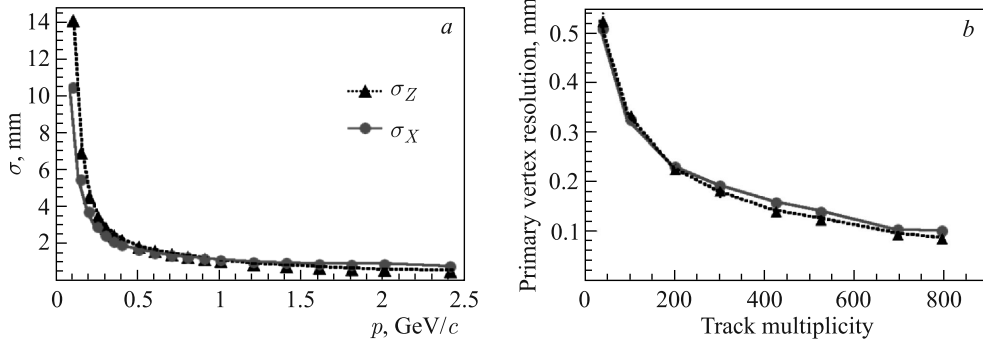


Fig. 5. *a*) Transverse and longitudinal position errors in the point of the closest approach (PCA) to the interaction point for TPC reconstructed primary tracks with $|\eta| < 1.3$ versus particle momentum; *b*) transverse and longitudinal position errors of the reconstructed primary vertex as functions of the track multiplicity

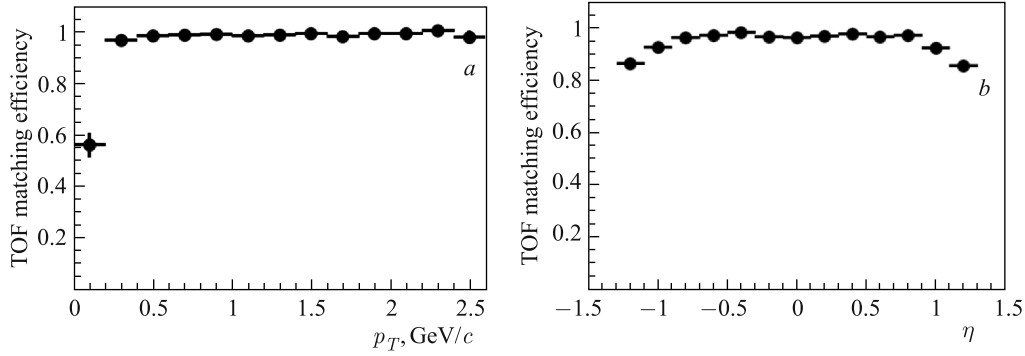


Fig. 6. *a*) TPC–TOF matching efficiency as a function of p_T ; *b*) the same as a function of η

to the corresponding TOF hits due to the interactions in the central electrode which divides the TPC gas volume into two drift regions; the matching deteriorates also toward the edge of the TOF at $|\eta| \approx 1.3$. The overall (integrated over p_T and $|\eta| < 1.3$) TPC–TOF matching efficiency is about 95%. For each TOF hit a Gaussian smearing of the time-of-flight provided by GEANT was done according to the design timing resolution of the TOF detector of 100 ps.

For the matched candidates the mass square (M^2) is derived through the relation

$$M^2 = \left(\frac{p}{q}\right)^2 \left(\frac{c^2 t^2}{l^2} - 1\right),$$

where p is the track momentum; q is its charge; t is the time-of-flight from TOF; l is the path length from the collision vertex to the TOF hit, and c is the speed of light. p/q , so-called magnetic rigidity, is the value directly returned by the track reconstruction algorithm. For particles with the unit charge it is equal to the momentum and M^2 corresponds to the particle mass squared. For multiple-charged particles the obtained value of M^2 differs from the nominal one by the factor of $1/q^2$, as can be seen, e.g., in Fig. 8 for ${}^3\text{He}$ (factor of 1/4 with respect to the expected squared mass of 9).

3.2. Particle Identification. Particle identification (PID) in the MPD experiment will be achieved in several ways. Hadrons (π, K, p) and light nuclei having no TOF hits can be identified using the energy loss (dE/dx) information from the TPC. As shown in Fig. 7, *a*, we can discriminate kaons from pions up to momenta of 0.7 GeV/ c and protons can be distinguished from π, K mesons up to $p \approx 1.3$ GeV/ c . Charged particles are selected if their dE/dx measurement lies within a $\pm 3\sigma$ interval around the predicted value which is taken from the Bethe–Bloch parameterization for the mean energy loss [32]. In Fig. 7, *b* an example of the MPD PID discrimination power using dE/dx is shown: the mean energy loss for tracks with momentum $p = 0.5$ GeV/ c is plotted in terms of Z variable defined as

$$Z = \ln \frac{dE/dx}{(dE/dx)_\pi}.$$

Particles within the pseudorapidity range $|\eta| < 1.1$ can be identified using the combined time-of-flight information from the TOF detector and the dE/dx signal from TPC. Figure 8, *a* shows a typical dE/dx versus M^2 distribution for tracks with momentum $p = 1.5$ GeV/ c .

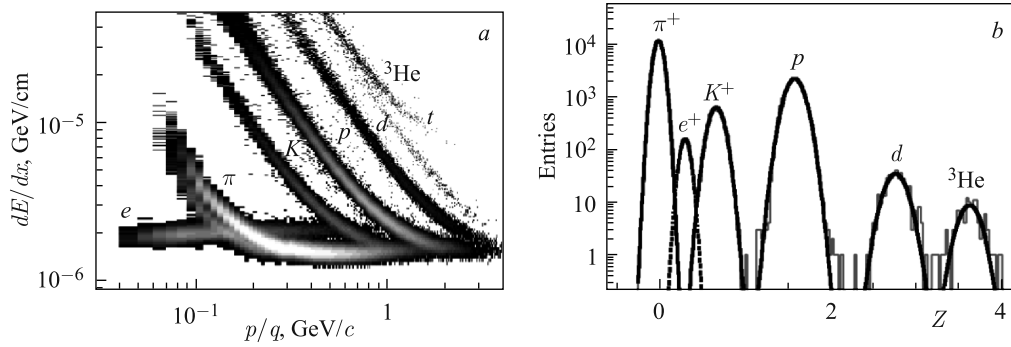


Fig. 7. *a*) Specific energy loss dE/dx versus magnetic rigidity p/q for $\pi, K, p, d, t, {}^3\text{He}$; *b*) a typical distribution of the Z value for tracks of 0.5 GeV/ c momentum with the Gaussian fits demonstrating the MPD particle separation

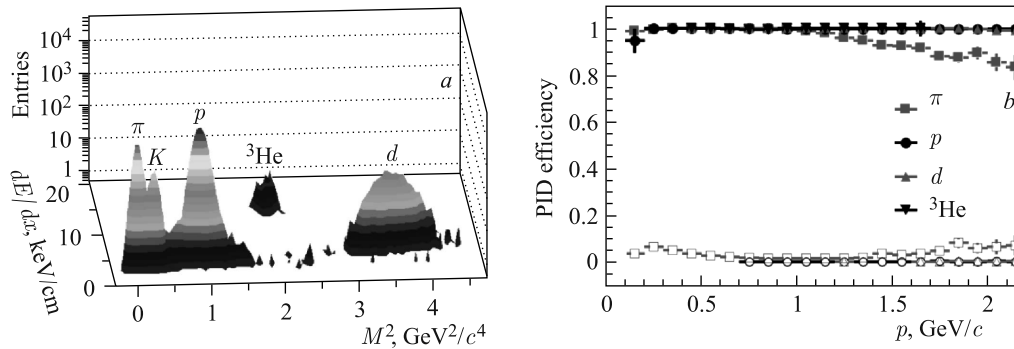


Fig. 8. *a*) Specific energy loss dE/dx versus mass square M^2 for $\pi, K, p, d, t, {}^3\text{He}$ at $p = 1.5$ GeV/ c ; *b*) PID efficiency (filled symbols) and contamination of misidentified particles (empty symbols) as functions of the total momentum

Selected hadron and light nuclei candidates fall within the 3σ ellipses around the nominal position for a given particle type. In addition, the probability for a given particle to belong to each of the species can be calculated knowing the widths of the corresponding distributions (along the dE/dx and M^2 axes) and the difference from the predicted position for the species. It was found that, by requiring this probability to be greater than 0.75, one can get the efficiency and contamination distributions shown in Fig. 8, *b*. The PID efficiency is defined as a ratio of the numbers of correctly tagged particles and all analyzed ones. The contamination is determined as the number of incorrectly tagged particles divided by the number of correctly tagged particles.

As seen from Fig. 8, the overall PID efficiency for p, d and ${}^3\text{He}$ is close to 100%, while due to a partial overlap of the distributions for pions and kaons the efficiency of π drops down to ≈ 0.8 at $p = 2.5 \text{ GeV}/c$. The contamination of wrongly identified pions (basically from $\mu, e,$ and K) does not exceed 10%. For other species the observed contribution from the misidentified particles is negligible.

4. ANALYSIS PROCEDURE

Λ ($\bar{\Lambda}$) hyperons and ${}^3\Lambda\text{H}$ hypernuclei were reconstructed using their decay modes into two ($\Lambda, \bar{\Lambda}, 2\text{-prong } {}^3\Lambda\text{H}$) or three (3-prong ${}^3\Lambda\text{H}$) charged tracks. The signal event topology (decay of a relatively long-lived particle into two or more tracks — Fig. 9) defines the selection criteria: relatively large distance of the closest approach (DCA) to the primary vertex of decay products, small track-to-track separation in the decay vertex, relatively large decay length of the mother particle. Obviously, the intertrack separation can be called a “quality” cut because it controls the secondary vertex reconstruction quality. In our selection procedure this criterion was complemented by another quality parameter — pointing angle, defined as the angle between the mother particle momentum and the direction vector from the primary to the secondary vertex. These cuts should be approximately the same for all particles under study. The other criteria (DCA and decay length) can be called the “topology” or rather “physics” cuts since they not only select the long-lived particle decay topology, but serve to reject background combinations. As such, they should depend on relative abundances of the signal particle decay products and background tracks within the detector acceptance (i.e., on the signal particle production cross section, branching fraction of the decay channel under consideration and phase space

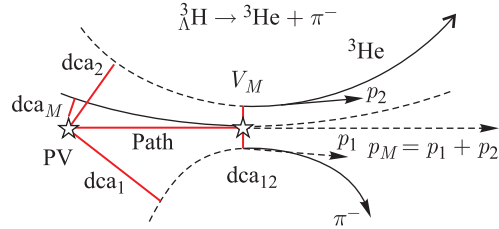


Fig. 9. Event topology of two-particle decays of a charged particle (e.g., ${}^3\Lambda\text{H} \rightarrow {}^3\text{He} + \pi^-$) (transverse view). Here dca_1 and dca_2 are the distances of the closest approach of the decay tracks to the primary vertex PV, dca_{12} is the distance between the daughter tracks in the decay vertex V_M , dca_M is the distance of the closest approach of the mother particle to the primary vertex, path is the decay length, p_1 and p_2 are the momenta of the daughter particles. Three-prong decays (${}^3\Lambda\text{H} \rightarrow d + p + \pi^-$) look similar to this one with the exception of a presence of the third decay particle, while two-particle decays of a neutral particle (e.g., $\Lambda \rightarrow p + \pi^-$) differ only in the mother particle trajectory which is a straight line in the latter case

Table 2. Selection cuts corresponding to the maximum significance of the invariant mass peak: χ_1^2 , χ_2^2 , χ_3^2 are the normalized to the number of degrees of freedom χ^2/NDF of decay tracks (from the lightest to the heaviest) with respect to the primary vertex, χ_V^2 is the secondary vertex fit quality, path is the decay length and angle is the pointing angle (see the text). Selected particle combinations should satisfy the following conditions: $\chi_1^2 > c_1$ && $\chi_2^2 > c_2$ (&& $\chi_3^2 > c_3$) && $\chi_V^2 < c_4$ && path $> c_5$ && angle $< c_6$, where c_i are the cut values

Particle	Selection cuts					
	χ_1^2	χ_2^2	χ_3^2	χ_V^2	Path, cm	Angle
K_S^0	4.5	5.5	—	3.5	1.3	0.17
Λ	3.8	3.0	—	2.8	2.6	0.09
$\bar{\Lambda}$	3.5	2.0	—	2.3	2.7	0.11
${}^3_\Lambda\text{H}$ (2-prong)	10.3	1.8	—	1.4	5.1	0.08
${}^3_\Lambda\text{H}$ (3-prong)	2.5	4.8	8.5	3.0	4.8	0.08

of decay products). Both the DCA and intertrack separation cuts should be more efficient if applied in χ^2 space, i.e., if normalized to their respective errors. However, this implies a good error analysis during the track reconstruction, which might not be the case at the early stage of the experiment. Therefore, for this analysis we used both sets of cuts, being aware of some redundancy of this collection of acceptance cuts. In fact, we have found that the normalized variables work quite well for our analysis and the obtained values of selections cuts are presented in Table 2.

The exact values of selection cuts were found by performing a multidimensional scan over the whole set of selection criteria with a requirement to maximize the invariant mass peak significance, defined as $S/\sqrt{S+B}$, where S and B are total numbers of signal (described by the Gaussian) and background (polynomial function) combinations inside $\pm 2\sigma$ interval around the peak position. While different physics analyses might prefer different criteria of the selection quality, the significance looks convenient to quantitatively evaluate the effect of different factors on the reconstruction quality.

The corresponding scan procedure was realized as follows: during the particle combinations the parameters which have been chosen to serve as selection criteria (see above) were recorded along with the invariant mass value. Later, multiple loops over those variables were performed in some steps and their values were used as low or high thresholds, yielding the invariant mass peak significance for each set of selection cut values. Then, the maximum value was taken along with the corresponding set of selection parameters.

5. RESULTS AND DISCUSSION

5.1. Reconstruction of K_S^0 Mesons. The results (Fig. 10) have been obtained for 10^4 central events, corresponding to about 30 s of data taking time. One can see that the reconstruction quality and efficiency will allow using the decay $K_S^0 \rightarrow \pi^+\pi^-$ as a convenient tool to monitor the tracking detector and track reconstruction performance being less dependent on the particle identification as compared to Λ decay.

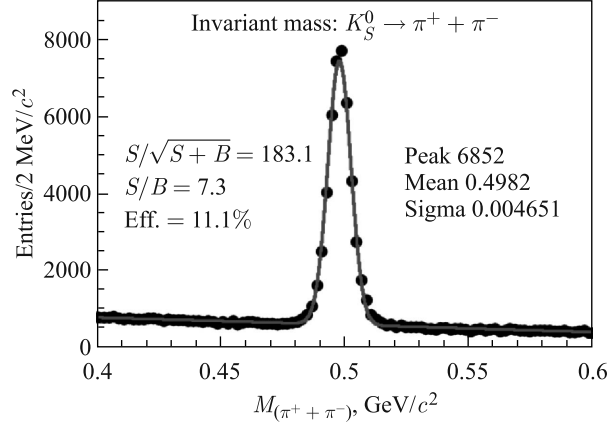


Fig. 10. Reconstructed invariant mass of π^+ and π^- . Also shown are the peak significance ($S/\sqrt{S+B}$), signal-to-background ratio (S/B), and efficiency (Eff.) inside $\pm 2\sigma$ interval around the peak position as well as the peak parameters from the Gaussian + polynom fit (peak, mean, sigma)

5.2. Reconstruction of Λ Hyperons. The results (Figs.11–14 and Table 3) have been obtained for 10^4 central events. As was already shown in Fig.2, the two event generators give somewhat different predictions on Λ production rate, rapidity, and p_T distributions. Moreover, these predictions are energy-dependent. Ideally, the experimentally measured quantities should reproduce these event features. Indeed, from Figs.11 and 12 one can see that even the reconstructed Λ yields reflect the UrQMD-DCM-QGSM differences, i.e., lower DCM-QGSM yield and softer p_T spectrum in the phase space covered by the detector can be explained by the lower production rate, wider rapidity, and softer p_T distributions of Λ hyperons in the full phase space (Fig. 2). More detailed information like rapidity distributions and p_T spectra confirms that the detector provides enough phase-space coverage to conserve the sensitivity to model predictions (cf. Figs. 2 and 13).

Table 3 shows the effect of the detector acceptance (i.e., η -coverage and low- p_T cut for Λ decay products) on hyperon detection efficiency, where the efficiency is defined with

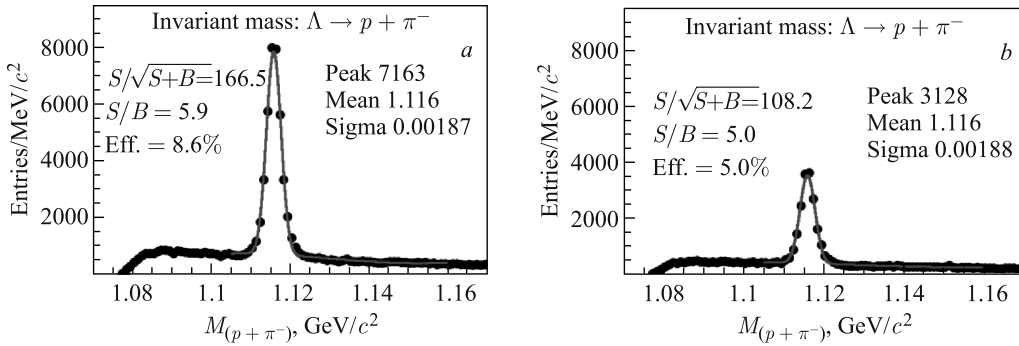


Fig. 11. Reconstructed invariant mass of proton and π^- for UrQMD (a) and DCM-QGSM (b) generators at $\sqrt{s} = 9A$ GeV (note the same vertical scale on both plots)

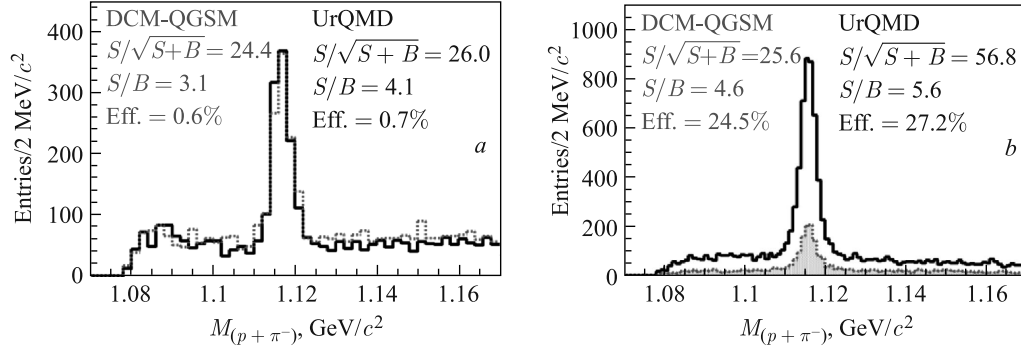


Fig. 12. Reconstructed invariant mass of proton and π^- for different p_T of the reconstructed object: *a*) $p_T < 0.5$ GeV/c; *b*) $1.5 < p_T < 2.0$ GeV/c. DCM-QGSM (gray color) and UrQMD (black color) generators at $\sqrt{s} = 9A$ GeV

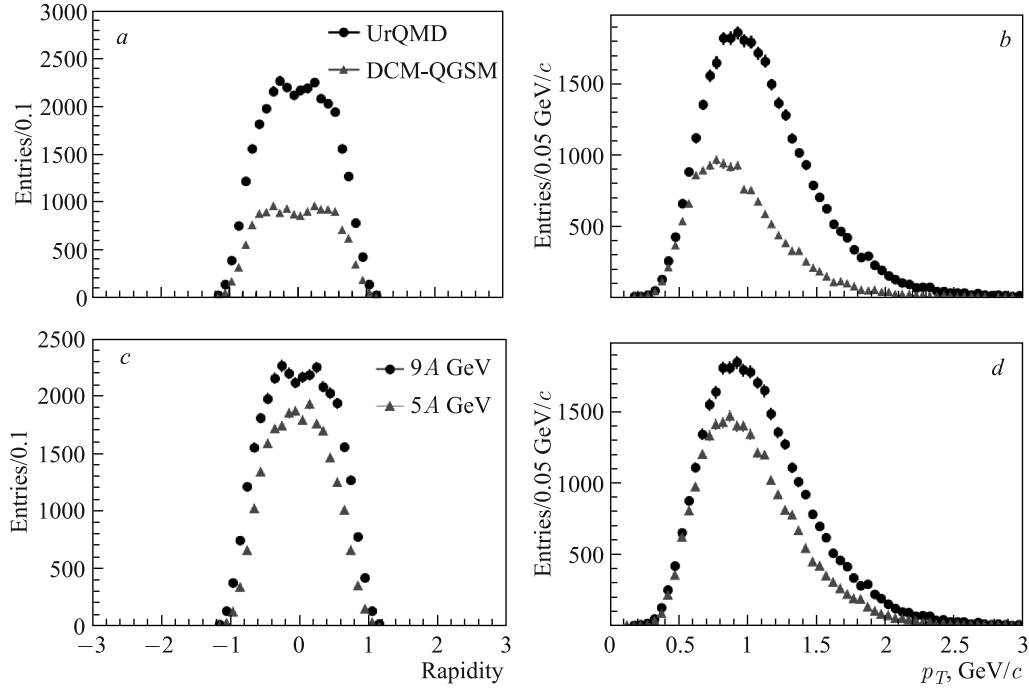


Fig. 13. *a, b*) Rapidity and p_T distributions of reconstructed Λ hyperons from UrQMD and DCM-QGSM generators at $\sqrt{s} = 9A$ GeV; *c, d*) rapidity and p_T distributions of reconstructed Λ hyperons from UrQMD generator at $\sqrt{s} = 5A$ and $9A$ GeV

respect to the total number of hyperons (as for Fig. 2). Lines 2–5 demonstrate the effect of the p_T cut on the efficiency, where p_T is the true transverse momentum of the decay pion and proton. Line 6 shows the reconstruction efficiency, i.e., considering the decay pions and protons reconstructed in the detector without any explicit p_T cut (and without PID efficiency).

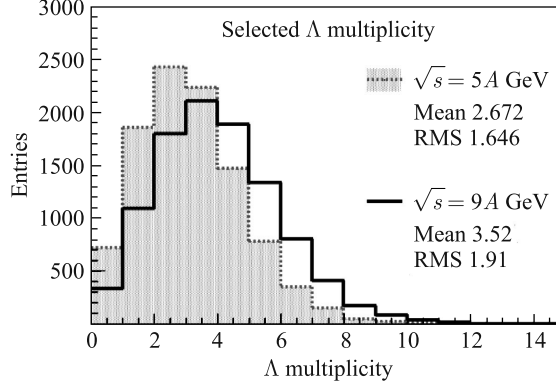


Fig. 14. Multiplicity of reconstructed Λ at $\sqrt{s} = 5A$ and $9A$ GeV from UrQMD generator

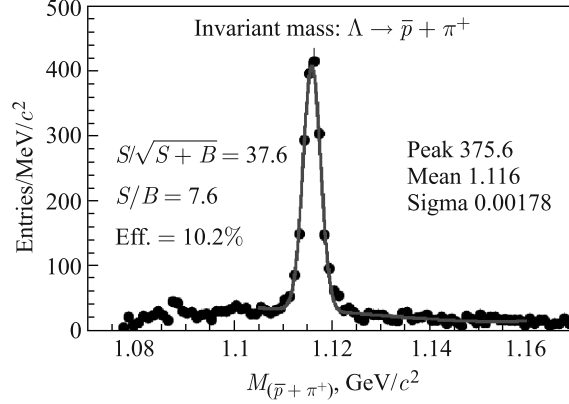
Table 3. Factors affecting Λ reconstruction efficiency

Factor	Efficiency, %			
	UrQMD (5A GeV)	DCM-QGSM (5A GeV)	UrQMD (9A GeV)	DCM-QGSM (9A GeV)
Branching ratio: $\Lambda \rightarrow p + \pi^-$	63.3	63.8	63.4	63.7
p and π^- at $ \eta < 1.3$	36.8	37.0	29.9	21.0
p and π^- at $ \eta < 1.3$ and $p_T > 0.05$ GeV/c	34.7	34.5	28.3	19.6
p and π^- at $ \eta < 1.3$ and $p_T > 0.1$ GeV/c	26.4	24.9	22.0	14.0
p and π^- at $ \eta < 1.3$ and $p_T > 0.2$ GeV/c	9.4	7.3	8.6	4.1
Reconstructed p and π^- at $ \eta < 1.3$	27.5	26.3	22.7	14.7
Maximum significance	9.8	8.9	8.6	5.0

The last line includes all the relevant factors, i.e., reconstruction and PID efficiencies as well as selection efficiency. One can see that the detector provides an efficient reconstruction of hyperons with p_T of decay tracks above 0.1 GeV/c in good agreement with Fig. 3. It is also clear that a higher p_T threshold (e.g., 0.2 GeV/c) would significantly reduce the detector efficiency. The efficiency drop due to selection cuts comes from the necessity to suppress the combinatorial background in order to obtain a clean invariant mass peak.

In Fig. 14 the multiplicity distributions of reconstructed Λ hyperons (per UrQMD event) are plotted for two collision energies. As one can see, the resulting efficiency will also allow studying some multiparticle phenomena with hyperons (for example, Λ - Λ correlations).

5.3. Reconstruction of $\bar{\Lambda}$ Hyperons. In Fig. 15 an invariant mass spectrum is shown calculated for pairs of antiprotons and positive pions. The results have been obtained for $4 \cdot 10^4$ central events, corresponding to about 2 min of data taking time. The peak of $\bar{\Lambda}$ is clearly seen and, inspite of a much lower production rate for antilambdas relative to the one for Λ ($\bar{\Lambda}/\Lambda \approx 10^{-2}$ in central Au + Au at $\sqrt{s} = 9A$ GeV), the obtained results for both the selection and total efficiencies are better than those for Λ (see Table 4). This is due to a higher fraction of antiprotons from weak decays in the total \bar{p} sample as compared to the proton case.

Fig. 15. Invariant mass spectrum of pairs of antiprotons and π^+ (UrQMD at $\sqrt{s} = 9A$ GeV)Table 4. Factors affecting $\bar{\Lambda}$ reconstruction efficiency

Factor	Efficiency, %
Branching ratio: $\bar{\Lambda} \rightarrow \bar{p} + \pi^+$	63.5
\bar{p} and π^+ at $ \eta < 1.3$	35.1
\bar{p} and π^+ at $ \eta < 1.3$ and $p_T > 0.05$ GeV/c	32.9
\bar{p} and π^+ at $ \eta < 1.3$ and $p_T > 0.1$ GeV/c	26.0
\bar{p} and π^+ at $ \eta < 1.3$ and $p_T > 0.2$ GeV/c	10.3
Reconstructed \bar{p} and π^+ at $ \eta < 1.3$	26.5
Maximum significance	10.3

5.4. Reconstruction of Hypernuclei ${}^3_{\Lambda}\text{H}$. The results (Fig. 16 and Table 5) have been obtained for $5 \cdot 10^5$ central events, corresponding to about 30 min of data taking time at NICA. Here it was necessary to suppress a larger combinatorial background as compared to the previous cases, and the requirement to have a sufficient significance of the signal resulted in stronger cuts and much lower efficiencies. Also, we observed a much larger drop in the overall reconstruction efficiency for hypertritons as compared to Λ hyperons (Tables 3 and 4)

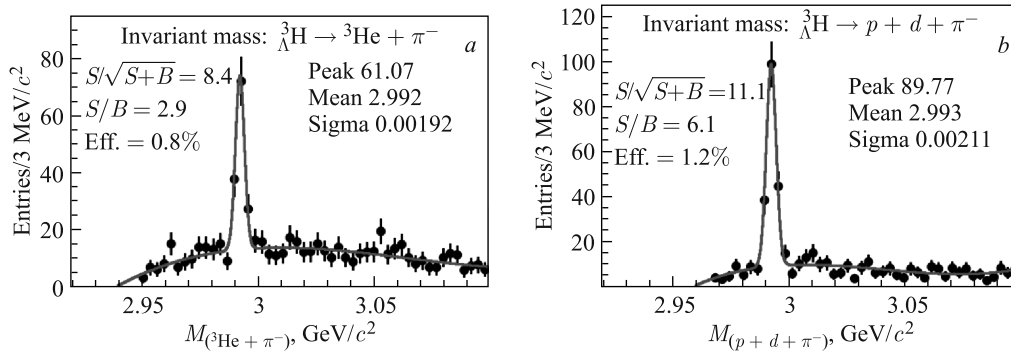
Fig. 16. a) Reconstructed invariant mass of ${}^3\text{He}$ and π^- ; b) reconstructed invariant mass of proton, deuteron, and π^- (DCM-QGSM generator at $\sqrt{s} = 5A$ GeV)

Table 5. Factors affecting ${}^3_{\Lambda}\text{H}$ reconstruction efficiency

Factor	Efficiency, %	
	2-prong decay	3-prong decay
Branching ratio	24.6	36.4
Decay products at $ \eta < 1.3$	14.9	19.8
Decay products at $ \eta < 1.3$ and $p_T > 0.05$ GeV/c	14.2	15.7
Decay products at $ \eta < 1.3$ and $p_T > 0.1$ GeV/c	8.9	6.2
Decay products at $ \eta < 1.3$ and $p_T > 0.2$ GeV/c	0.7	0.1
Reconstructed decay products at $ \eta < 1.3$	7.9	8.3
Maximum significance	0.8	1.2

when the low- p_T cut-off of decay products increased from 0.1 to 0.2 GeV/c. Therefore, the MPD detector ability to reconstruct very low momentum particles (at least, down to $p_T = 0.1$ GeV/c) is of crucial importance for measurements of hypernuclei. One can notice in Table 2 a large difference of χ^2_1 values (χ^2 of decay π^- with respect to the primary vertex) for 2- and 3-prong decays, confirming the considerations presented in Sec. 4.

6. SUMMARY AND PLANS

We have performed a simulation study of the MPD detector capabilities to reconstruct K^0 mesons, (anti-) Λ , and hypertritons in central Au + Au collisions at $\sqrt{s} = 5A$ and $9A$ GeV. Two event generators (UrQMD and DCM-QGSM) were used as the input for the study of the MPD detector set-up comprising the Time Projection Chamber and barrel Time-Of-Flight system. Particle identification was achieved by combining the energy loss (from TPC) and time-of-flight (from TOF) measurements. A special procedure aimed at the maximization of the significance of the reconstructed invariant mass was developed resulting in the observed signal-to-background ratio $S/B \approx 6$ for Λ and $S/B = 3-6$ for hypertritons. The invariant mass resolution of ≈ 2 MeV/c² (for (anti-) Λ and hypertritons) and ≈ 5 MeV/c² (for K^0) has been achieved. Based on the results of this study and model predictions, we have estimated the expected yields of particle species of interest for 10 weeks of data taking (see Table 6).

Table 6. Expected particle yields for 10 weeks of running time

Particle	Expected yield			
	UrQMD (5A GeV)	DCM-QGSM (5A GeV)	UrQMD (9A GeV)	DCM-QGSM (9A GeV)
Λ	$4.3 \cdot 10^9$	$3.4 \cdot 10^9$	$5.8 \cdot 10^9$	$2.5 \cdot 10^9$
$\bar{\Lambda}$			$7.3 \cdot 10^7$	
${}^3_{\Lambda}\text{H}$		$9.1 \cdot 10^5$		

It is also planned to evaluate the detector capabilities to reconstruct rarer strange probes like Ξ , Ω , and ${}^4_{\Lambda\Lambda}\text{H}$ [33].

Acknowledgements. The authors are grateful to E. V. Kuznetsova for help in the preparation of the paper.

REFERENCES

1. *Sissakian A. N. (NICA Collab.)*. The Nuclotron-Based Ion Collider Facility (NICA) at JINR: New Prospects for Heavy Ion Collisions and Spin Physics // *J. Phys. G: Nucl. Part. Phys.* 2009. V. 36. P. 064069.
2. *Rapp R., Chanfray G., Wambach J.* Medium Modifications of the Rho Meson at CERN SPS Energies // *Phys. Rev. Lett.* 1996. V. 76. P. 368.
3. *Rapp R., Wambach J.* Chiral Symmetry Restoration and Dileptons in Relativistic Heavy Ion Collisions // *Adv. Nucl. Phys.* 2000. V. 25. P. 1.
4. *Hatsuda T., Lee S.H.* QCD Sum Rules for Vector Mesons in Nuclear Medium // *Phys. Rev. C.* 1992. V. 46. P. 34.
5. *Alt C. (NA49 Collab.)*. Pion and Kaon Production in Central Pb+Pb Collisions at 20A and 30A GeV: Evidence for the Onset of Deconfinement // *Phys. Rev. C.* 2008. V. 77. P. 024903.
6. *Kumar L. (STAR Collab.)*. Identified Hadron Production from the RHIC Beam Energy Scan // *J. Phys. G: Nucl. Part. Phys.* 2011. V. 38. P. 124145.
7. *Randrup J., Cleymans J.* Maximum Freeze-Out Baryon Density in Nuclear Collisions // *Phys. Rev. C.* 2006. V. 74. P. 047901.
8. http://nica.jinr.ru/files/NICA_CDR.pdf
9. *Abraamyan K. U. (MPD Collab.)*. The MPD Detector at the NICA Heavy-Ion Collider at JINR // *Nucl. Instr. Meth. A.* 2011. V. 628. P. 99.
10. http://nica.jinr.ru/files/CDR_MPD/MPD_CDR_en.pdf
11. *Rafelski J., Muller B.* Strangeness Production in the Quark-Gluon Plasma // *Phys. Rev. Lett.* 1982. V. 48. P. 1066.
12. *Antinori F. (WA97 Collab.)*. Strangeness Enhancement at Mid-Rapidity in Pb–Pb Collisions at 158A GeV/c: A Comparison with VENUS and RQMD Models // *Eur. Phys. J. C.* 1999. V. 11. P. 79.
13. *Antinori F. (NA57 Collab.)*. Enhancement of Hyperon Production at Central Rapidity in 158A GeV/c Pb–Pb Collisions // *J. Phys. G.* 2006. V. 32. P. 427.
14. *Adamczyk L. (STAR Collab.)*. Elliptic Flow of Identified Hadrons in Au + Au Collisions at $\sqrt{s_{NN}} = 7.7\text{--}62.4$ GeV // *Phys. Rev. C.* 2013. V. 88. P. 014902.
15. *Kerman A. K., Weiss M. S.* Superstrange Nuclei // *Phys. Rev. C.* 1973. V. 8. P. 408.
16. *The STAR Collab.* // *Science.* 2010. V. 328. P. 58.
17. *Dönigus B. (ALICE Collab.)*. (Anti-)Matter and Hyper-Matter Production at the LHC with ALICE // *Nucl. Phys. A.* 2013. V. 904–905. P. 547.
18. *Wakai M., Bando H., Sano M.* Hypernucleus Formation in High-Energy Nuclear Collisions // *Phys. Rev. C.* 1988. V. 38. P. 748.
19. *Andronic A. et al.* Production of Light Nuclei, Hypernuclei and Their Antiparticles in Relativistic Nuclear Collisions // *Phys. Lett. B.* 2011. V. 697. P. 203.
20. *Steinheimer J. et al.* Hypernuclei, Dibaryon and Antinuclei Production in High Energy Heavy Ion Collisions: Thermal Production versus Coalescence // *Phys. Lett. B.* 2012. V. 714. P. 85.
21. <http://urqmd.org/>
22. *Toneev V. D., Gudima K. K.* Particle Emission in Light and Heavy Ion Reactions // *Nucl. Phys. A.* 1983. V. 400. P. 173.
23. *Toneev V. D. et al.* Dynamics of Relativistic Heavy Ion Collisions // *Nucl. Phys. A.* 1990. V. 519. P. 463.

24. *Amelin N. S. et al.* Further Development of a Quark-Gluon String Model for Describing High-Energy Collisions with a Nuclear Target // *Sov. J. Nucl. Phys.* 1990. V. 52. P. 272.
25. *Botvina A. S. et al.* Production of Spectator Hypermatter in Relativistic Heavy-Ion Collisions // *Rhys. Rev. C.* 2011. V. 84. P. 064904.
26. *Botvina A. S., Pochodzalla J.* Production of Hypernuclei in Multifragmentation of Nuclear Spectator Matter // *Phys. Rev. C.* 2007. V. 76. P. 024909.
27. *Armstrong T. A. (E864 Collab.)*. Mass Dependence of Light Nucleus Production in Ultrarelativistic Heavy Ion Collisions // *Phys. Rev. Lett.* 1999. V. 83. P. 5431.
28. *Armstrong T. A. (E864 Collab.)*. Measurements of Light Nuclei Production in 11.5A GeV/c Au + Pb Heavy Ion Collisions // *Phys. Rev. C.* 2000. V. 61. P. 064908.
29. *Kamada H. et al.* Pi Mesonic Decay of the Hypertriton // *Phys. Rev. C.* 1998. V. 57. P. 1595.
30. *Fruhvirth R.* Application of Kalman Filtering to Track and Vertex Fitting // *Nucl. Instr. Meth. A.* 1987. V. 262. P. 444.
31. *Luchsinger R., Grab Ch.* Vertex Reconstruction by Means of the Method of Kalman Filter // *Comp. Phys. Commun.* 1993. V. 76. P. 263.
32. *Beringer J. (Particle Data Group)*. Review of Particle Physics // *Phys. Rev. D.* 2012. V. 86. P. 010001.
33. *Kumagai-Fuse I., Okabe Sh.* Pionic Weak Decay of the Lightest Double Lambda Hypernucleus Lambda-Lambda H-4 // *Phys. Rev. C.* 2002. V. 66. P. 014003.

Received on June 2, 2014.